J Mater Sci (2011) 46:3258–3268
DOI 10.1007/s10853-010-5213-x

Thermo-mechanical and microstructural issues in dissimilar friction stir welding of AA5086–AA6061

H. Jamshidi Aval · S. Serajzadeh · A. H. Kokabi

Received: 4 July 2010 / Accepted: 20 September 2010 / Published online: 5 January 2011

Abstract In this research, thermo-mechanical behavior and microstructural events in dissimilar friction stir welding of AA6061-T6 and AA5086-O have been evaluated. The thermo-mechanical responses of materials during the process have been predicted employing a three-dimensional model together with a finite element software, ABAQUS. Then, mechanical properties and microstructures of the weld zone were studied with the aid of experimental observations and model predictions. It is found that the mixing of material in the weld nugget is performed more efficiently when AA5086 is in the advancing side and also the temperature field is distributed asymmetrically resulting in larger thermally affected region in the AA6061 side. Besides, the microstructural studies shows that the microstructures of stirred zone consist of fine equiaxed grains where finer grains are produced in AA6061 side compared to AA5086 side.

Introduction

Friction stir welding (FSW) is a significant manufacturing process in solid-state welding operations [1]. Many types of materials can be joined by this process and accordingly, most of workable aluminum alloys can be welded by this process including those that cannot normally be employed in conventional fusion welding techniques. In this process, a specially shaped cylindrical tool rotates and plunges into the work-piece until shoulder of the tool touches the work-piece surface and then the rotating tool moves at a constant velocity along the welding line. Rotary motion of the shoulder generates frictional heat producing softened region around the pin while the shoulder prevents deforming material from being flowed outward. As a result, a weld joint is made by extrusion of thermally softened material from the leading side to the trailing side of the rotating tool [2]. The solid-state nature of FSW provides several advantages comparing to the conventional fusion welding methods additionally, the joining occurs by the plastic flow of material at temperatures lower than the melting temperature of base metal and thus it is possible to avoid solidification related problems occurred in the arc welding of metals and alloys.

Many attempts have been made to study the process FSW in various alloys. For example, Woo et al. [3] have proposed a method that can predict the minimum hardness location as a function of natural aging time after friction stir welding of AA6061-T6. It is found that the minimum hardness location moves away from the weld centerline as the aging time increases. Safarkhanian et al. [4] have considered the effect of the abnormal grain growth on the tensile strength of friction stir welded AA2024-T4. It was reported that if abnormal grain growth completely occurs in stirred zone the tensile strength and elongation of the heat treated joint increases significantly. Zhou et al. [5] have investigated the effect of process variables on the stirred zone microstructures in friction stir welds of Ti–6Al–4V. They have reported that the stirred zone microstructures can be controlled efficiently by selecting the appropriate rotational and welding speeds. Venkateswaran et al. [6] have studied mechanical properties of dissimilar friction stir welded AA6061 and AZ31B magnesium alloy. According to X-ray diffraction and fractography results of the tensile fracture surfaces they have shown that the

H. Jamshidi Aval · S. Serajzadeh (✉) · A. H. Kokabi
Department of Materials Science and Engineering, Sharif University of Technology, Azadi Ave, PO Box 11155-9466, Tehran, Iran
e-mail: serajzadeh@sharif.edu

failure of the Al–Mg dissimilar weld joints occurs through the brittle intermetallic layer (Al_3Mg_2 and $Al_{12}Mg_{17}$) present at the interface. Chen [7] has studied on optimum operating conditions of dissimilar friction stir welding of AA6061 aluminum alloy and SS400 low-carbon steel. He has shown that the transverse speed of 0.9 mm/s combined with a rotational speed of 550 rpm results in the best quality for impact properties and provides an acceptable quality of tensile strength.

The dissimilar friction stir welding of aluminum alloys has also been considered in a few researchers. For instance; Leal et al. [8] have examined the effect of shoulder geometry on material flow during dissimilar friction stir welding of AA5182-H111 and AA6016-T4. They have reported that pin-driven flow is predominant when the conical cavity shoulder is used, however, the interaction between pin-driven and shoulder-driven flow is different. Lee et al. [9] have studied dissimilar lap joint friction stir welded AA5052-H112 and AA6061-T6 under different welding parameters. It is reported that the mechanical strength of the joint is affected by interface geometry. Also, they have shown that fracture load decreases at higher rotational and lower welding speeds. Shigematsu et al. [10] have investigated friction stir welding of dissimilar AA6061–AA5083. They have reported that welding properties such as the hardness distribution and the tensile strength were strongly influenced by the material combination. Larsson et al. [11] have investigated dissimilar I-joints FSW of AA5083-H12 and AA6082-T6. They have shown that the material with lower flow stress should be placed at the advancing side and higher traveling speeds are found to be more suitable. Peel et al. [12, 13] have studied dissimilar friction stir welding in AA5083–AA6082. They have considered the impact of changes in the rotation and traverse speed on the process parameters. It was reported that the effect of rotational speed on the temperature close to the weld line is more than the traverse speed. Steuwer et al. [14] have considered the effect of process parameters on residual stress in dissimilar friction stir welding of AA5083–AA6082. It is found that the rotational speed of the welding tool is more effective than the transverse speed on the residual stresses in the welds particularly on the AA5083 side.

Although, a few works have been conducted to investigate the dissimilar friction stir welding of aluminum alloys, however, more studies are still necessary to evaluate the materials responses during friction stir welding of aluminum alloys. In this study, the effect of welding arrangement and process parameters in friction stir welding of AA5086-O and AA6061-T6 are considered and the developed microstructures in weld zone and the mechanical properties of the welded samples are investigated. Accordingly, a three-dimensional model is performed to determine temperature, strain rate and strain distributions during welding as well as microstructural and mechanical testing are conducted to evaluate the effect of process parameters on welded materials.

Mathematical model

The contact friction and plastic deformation of the material are the main heat source in the friction stir welding process. Therefore, to include the effect of temperature on flow behavior of metal being deformed, both thermal and mechanical solutions must be determined simultaneously. Accordingly, a coupled thermal-stress analysis is used in determination of thermal and mechanical responses during friction stir welding process employing ABAQUS/Explicit [15]. To determine the velocity field, the energy functional should be minimized as below [16]:

$$\delta\pi = \int_V \rho\ddot{\mathbf{u}} \cdot \delta\mathbf{v}\mathrm{d}V + \int_V \boldsymbol{\sigma} : \delta\mathbf{D}\mathrm{d}V - \int_S \mathbf{F} \cdot \delta\mathbf{v}\mathrm{d}S = 0 \quad (1)$$

where "V" denotes the volume of deforming body, and "S" is boundary surface. $\ddot{\mathbf{u}}$, $\delta\mathbf{v}$ and $\boldsymbol{F}$ are the acceleration, virtual velocity, and traction vectors, respectively. $\boldsymbol{\sigma}$ is Cauchy stress tensor, $\delta\mathbf{D}$ is the virtual deformation rate tensor and ρ is density. The finite element form of the above equation can be described as below [16]:

$$\mathbf{M}\ddot{\mathbf{u}} + \mathbf{F}_{\mathrm{int}} = \mathbf{F}_{\mathrm{ext}} \quad (2)$$

where $\mathbf{M}$ is the mass matrix, $\boldsymbol{F}_{\mathrm{int}}$ and $\boldsymbol{F}_{\mathrm{ext}}$ are internal and external force vectors, respectively. "$\ddot{\mathbf{u}}$" expresses nodal acceleration vector. The nodal displacement vector can be explicitly determined in each time step using the lumped mass matrix as below:

$$\ddot{\mathbf{u}}^n = \mathbf{M}^{-1}\left(\mathbf{F}_{\mathrm{ext}}^n - \mathbf{F}_{\mathrm{int}}^n\right) \quad (3)$$

here "n" denotes the current time step. Then, using the central difference scheme the displacement vector is determined as:

$$\mathbf{v}^{n+1/2} = \Delta t\mathbf{M}^{-1}\left(\mathbf{F}_{\mathrm{ext}}^n - \mathbf{F}_{\mathrm{int}}^n\right) + \mathbf{v}^{n-1/2} \quad (4)$$

$$\mathbf{u}^{n+1} = \mathbf{u}^n + \Delta t\mathbf{v}^{n+1/2} \quad (5)$$

Thermal response of the material should also be calculated at the same time because of interconnection between mechanical and thermal behaviors of metal being deformed. The governing heat conduction equation may be expressed as below:

$$\frac{\partial}{\partial x}\left(k\frac{\partial T}{\partial x}\right) + \frac{\partial}{\partial y}\left(k\frac{\partial T}{\partial y}\right) + \frac{\partial}{\partial z}\left(k\frac{\partial T}{\partial z}\right) + \dot{Q} = \rho c_{\mathrm{p}}\frac{\partial T}{\partial t} \quad (6)$$

where c_{p} is the heat capacity, k the thermal conductivity, T temperature, and $\dot{Q}$ is the rate of heat generation calculated

Table 1 The physical material properties and young's modulus of AA5086 and AA6061 used in this work [20, 21]

	Density (kg/m^3)	Thermal expansion		Thermal cond.		Heat capacity		Young's modulus	
		(10^{-6}/°C)	Temp (°C)	(W/m °C)	Temp (°C)	(J/g °C)	Temp (°C)	(GPa)	Temp (°C)
AA5086	2657	23.8	25	127	25	0.900	25	70 .0	25
		25.5	200	151	250	0.960	250	67.8	100
		26.8	300	154	300	0.980	300	60.7	200
		28.9	400	158	400	1.020	400	51.0	300
		31.5	500	169	500	1.113	500	37.4	400
AA6061	2700	23.4	25	167	25	0.896	25	68.5	25
		24.6	100	180	100	0.978	100	66.1	100
		25.6	150	184	150	1.004	150	63.1	150
		26.6	200	192	200	1.028	200	59.1	200
		27.5	250	201	250	1.052	250	54.0	250
		28.5	300	207	300	1.078	300	46.4	300
		30.7	450	230	450	1.133	450	31.7	450

Table 2 The alloys composition (wt%)

	Mg	Mn	Cu	Cr	Si	Fe	Al
AA5086	4.12	0.447	0.030	0.105	0.244	0.343	Balancing
AA6061	0.918	0.083	0.328	0.065	0.663	0.491	Balancing

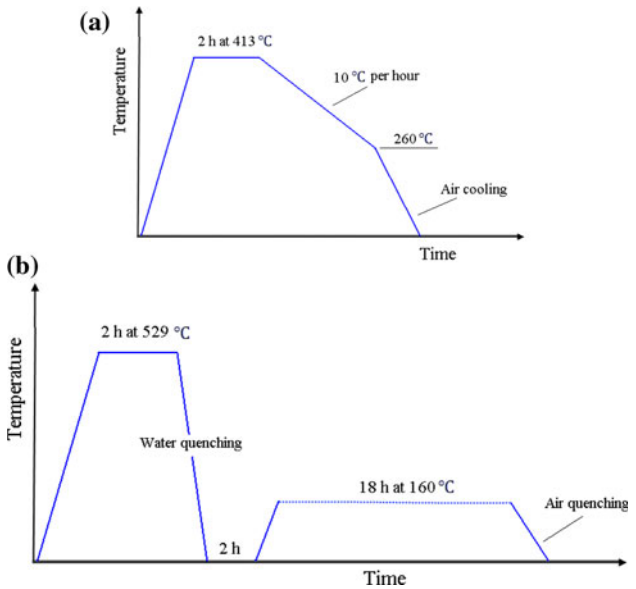

Fig. 1 Heat treatment of AA6061: **a** annealing, **b** solution heat treatment and artificially ageing

from the deformation model. *x*-axis represents welding direction, *y*-axis transverse direction, and *z*-axis thickness direction. Utilizing finite element formulation together with forward difference scheme, the nodal temperature in each time step is calculated as follows [17]:

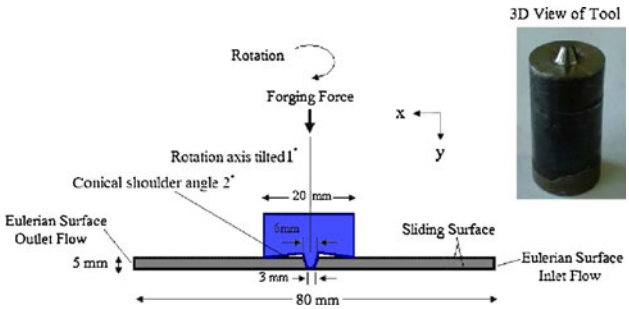

Fig. 2 Schematic view of numerical setup and tool specifications

$$\mathbf{T}^{n+1} = \Delta t \mathbf{C}^{-1}(\mathbf{Q}^n - \mathbf{K}^n\mathbf{T}^n) + \mathbf{T}^n \tag{7}$$

here **C**, **K**, and ***Q*** are capacitance matrix, stiffness matrix, and heat vector, respectively, and "*n*" represents the time step. Since both thermal and mechanical models are handled by explicit techniques, i.e., the forward difference for the thermal analysis and central difference for the mechanical part therefore, the mechanical and the thermal solutions are obtained simultaneously by an explicit coupling. In other words, no iterations or tangent stiffness matrices are required in the solution. Note that central and forward difference operators are conditionally stable and the maximum time step for a stable solution is determined as below [15];

$$\Delta t \leq \min\left(\frac{2}{\omega_{\max}}, \frac{2}{\lambda_{\max}}\right) \tag{8}$$

where $\omega_{\max}$ is the highest frequency in the system of equations of the mechanical solution and $\lambda_{\max}$ is the largest eigenvalue in the system of equations relating to the thermal solution. In this regard, using a mass scaling algorithm may be useful ensuring a stable computational

procedure with reasonable run-time duration. To solve the heat conduction problem, three-dimensional Cartesian coordinate system is employed and the initial and boundary conditions considered in this model are based on the actual conditions as follows. The shoulder/work-piece and pin/work-piece interface are subjected to the imposed heat flux as below [18]:

$$k\frac{\partial T}{\partial n}\bigg|_{S,p} = \mu p\dot{\gamma} \tag{9}$$

where μ is the friction coefficient, p the contact pressure, and $\dot{\gamma}$ is the slip rate where this parameter is determined using the predicted velocity field in each time step. Friction behavior is modeled by Coulomb friction model while the Coulomb's friction coefficient is defined as a function of slip rate, contact pressure, and surface temperature. In addition, convection–conduction boundary conditions are utilized at the surface boundaries, while the convective heat transfer coefficient are assumed to be as 1000 W m^{-2} K^{-1} in the regions that are in contact with backing plate and this parameter is taken as 20 W m^{-2} K^{-1} elsewhere. Because of a balance between model accuracy and model size only a specific part of the work-pieces is included having diameter of 80 mm. It is worth nothing that the interface of the work-pieces is modeled as an Eulerian surface. The three-dimensional thermal coupled elements, C3D8RT, are employed in the finite element solution and each part of the weldment, AA6061 and AA5086, is discretized into 15510 three-dimensional elements containing 18546 nodes. The mesh structure is constructed in the cylindrical coordinates system, therefore the element width in the angular direction near the center is smaller than those at larger radii. Adaptive mesh scheme is also utilized in Abaqus/Explicit to handle severe element distortion. In the mechanical model, top and bottom surfaces and contact surface between pin and work-pace are assumed as sliding surfaces and the other surfaces are taken as Euleraian ones. The sliding surface has a Lagrange type while this type of meshes follows the material movement. Because of complexity in modeling of dissimilar material mixing around pin and tool shoulder, the material flowing into an Eulerian boundary region is assumed to have the same physical and mechanical properties as the material that is inside the adaptive mesh domain. Therefore, the temperature and velocity fields around tool and shoulder both in AA6061 and AA5086 are predicted under actual conditions,

Table 3 Welding parameter used in the experiments

Designation	Material		Rotational speed (rpm)	Welding speed (cm/min)
	Advancing	Retreating		
A	AA6061-T6	AA5086-O	840	10
B	AA6061-T6	AA5086-O	840	15
C	AA6061-T6	AA5086-O	900	10
D	AA6061-T6	AA5086-O	900	15
E	AA6061-T6	AA5086-O	1000	10
F	AA6061-T6	AA5086-O	1000	15
G	AA6061-T6	AA5086-O	1200	10
H	AA6061-T6	AA5086-O	1200	15
I	AA5086-O	AA6061-T6	840	10
J	AA5086-O	AA6061-T6	840	15
K	AA5086-O	AA6061-T6	900	10
L	AA5086-O	AA6061-T6	900	15
M	AA5086-O	AA6061-T6	1000	10
N	AA5086-O	AA6061-T6	1000	15
O	AA5086-O	AA6061-T6	1200	10
P	AA5086-O	AA6061-T6	1200	15
Q	AA5086-O	AA6061-T6	600	10
R	AA5086-O	AA6061-T6	600	15
S	AA6061-T6	AA5086-O	600	10
T	AA6061-T6	AA5086-O	600	15

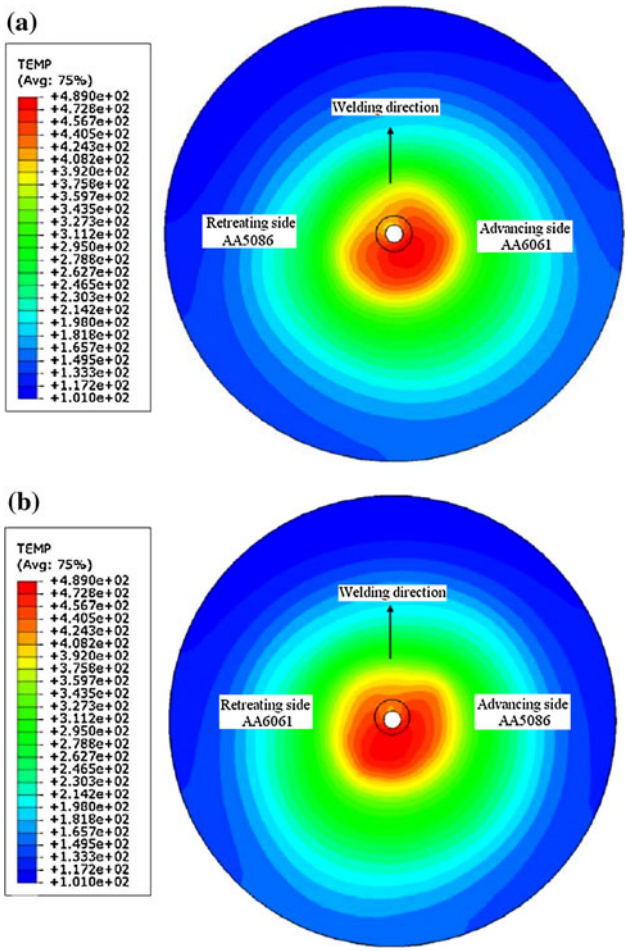

Fig. 3 Predicted temperature field after 15 s for samples; **a** sample D, **b** sample L

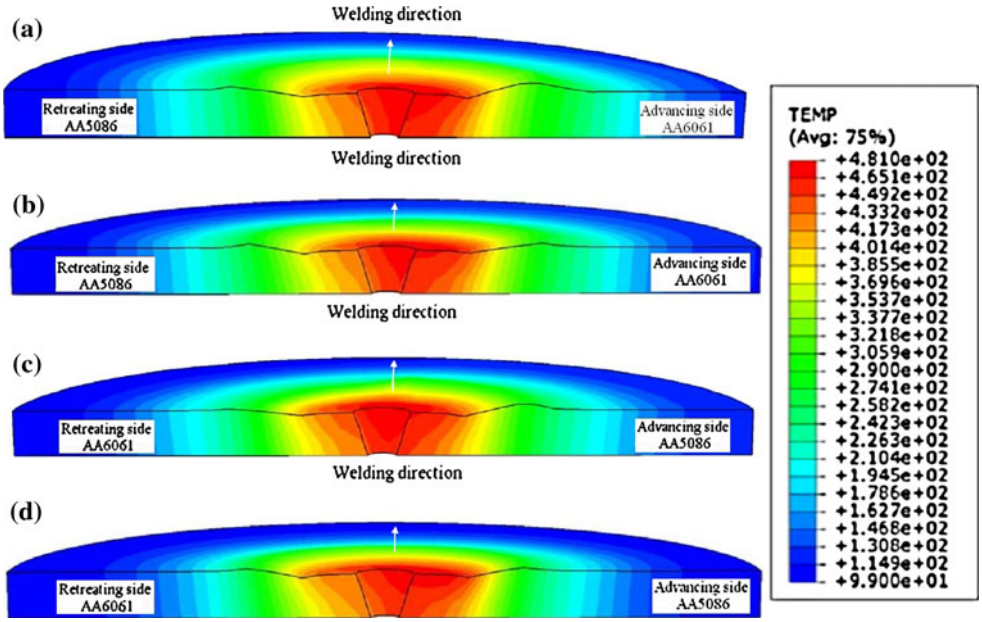

Fig. 4 Predicted temperature field after 15 s in the transversal cross-section near the tool/work-piece interface; **a** sample A, **b** sample B, **c** sample I, **d** sample J

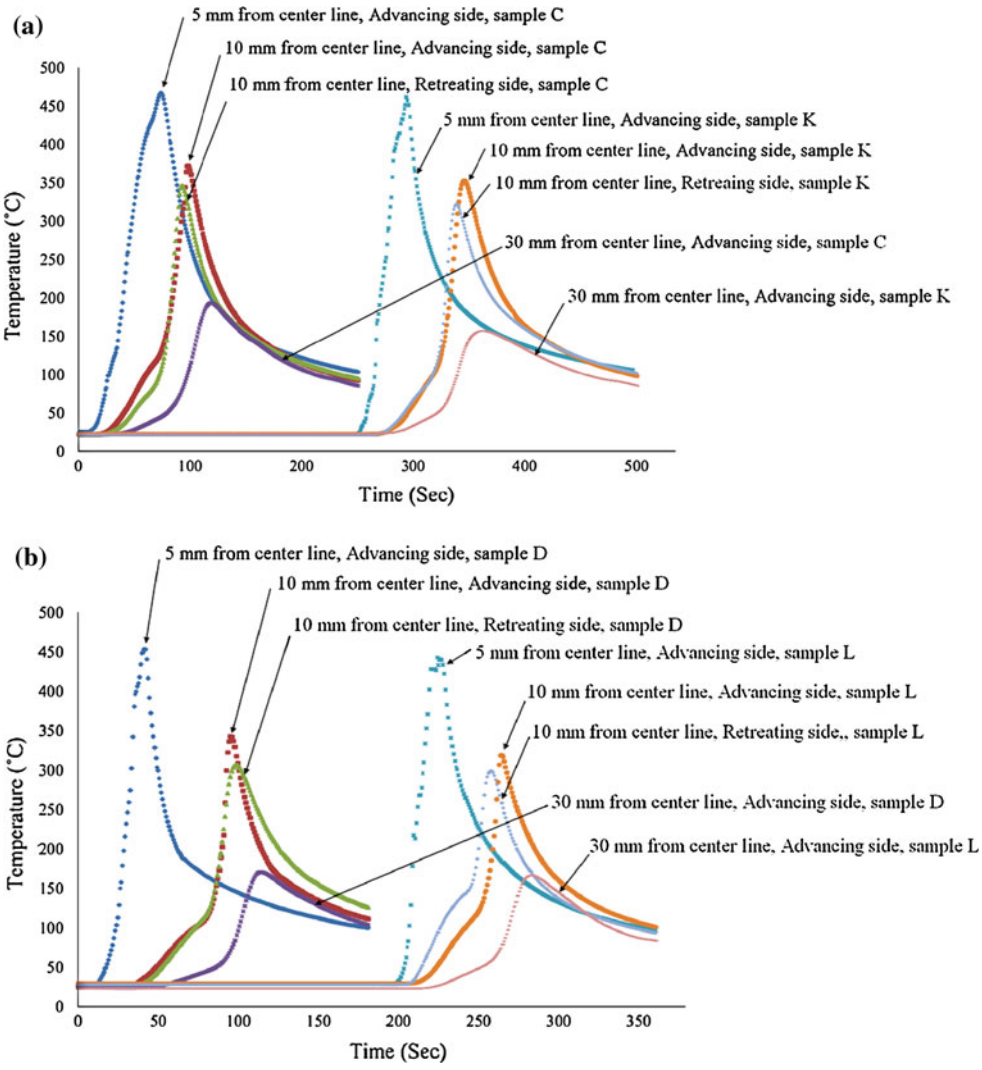

Fig. 5 Measured thermal cycles in the various samples with similar welding parameters; **a** sample C and K, **b** sample D and L

however, because of complexity in definition of an element with the mixed mechanical and physical properties, it is assumed that mixing of material in weld seem is not occurred. Although, this assumption somehow affects the thermo-mechanical responses of nugget zone, however, behavior of thermo-mechanically affected zone and HAZ can be modeled more accurately. Moreover, flow stress behaviors of the employed materials are determined using the data presented in Ref. [19] while the physical material properties and Young modulus of AA5086-O and AA6061-T6 are given in Table 1 using the data published in Refs. [20, 21].

Experimental procedures

Friction stir welding experiments were conducted on samples of AA5086-O and AA6061-T6 with the composition listed in Table 2. In the experiments, two cases were investigated: (a) AA5086-O on the advancing side and AA6061-T6 on the retreating side, and (b) AA6061-T6 on the advancing side and AA5086-O on the retreating side. The plates with 5-mm thickness were cut out of the raw material and AA5086 was annealed at 345 °C for 1.5 h while AA6061 was first annealed and solution heat treated and then artificially aged as shown in Fig. 1. Single-pass friction stir butt welds were performed using a tool with a shoulder of 20 mm in diameter and conical pin while the inclination angle was set to 1°. The dimensions of tool are shown in Fig. 2 and the employed welding parameters are listed in Table 3. In addition, the temperature variations in different positions were recorded during welding experiments using K-type thermocouples. Three thermocouples in the advancing side at distance of 5, 10, 30 mm from weld line and one thermocouple in the retreating side at distance of 10 mm from weld line were inserted. Optical metallography and SEM studies have been performed on welded samples. A reagent made of 0.5 mL HF, 15.5 mL HNO_3, 84 mL H_2O, and 0.3 g Cr_2O_3 was used to etch the AA5086 side and a reagent made of 3 mL HNO_3, 6 mL HF, 6 mL HCl, and 150 mL H_2O was used to reveal the microstructures of the AA6061 side in all samples. The etched samples were examined by an optical microscope Olympus PME3 equipped a digital camera CLEMEX-BX51M. The Vickers

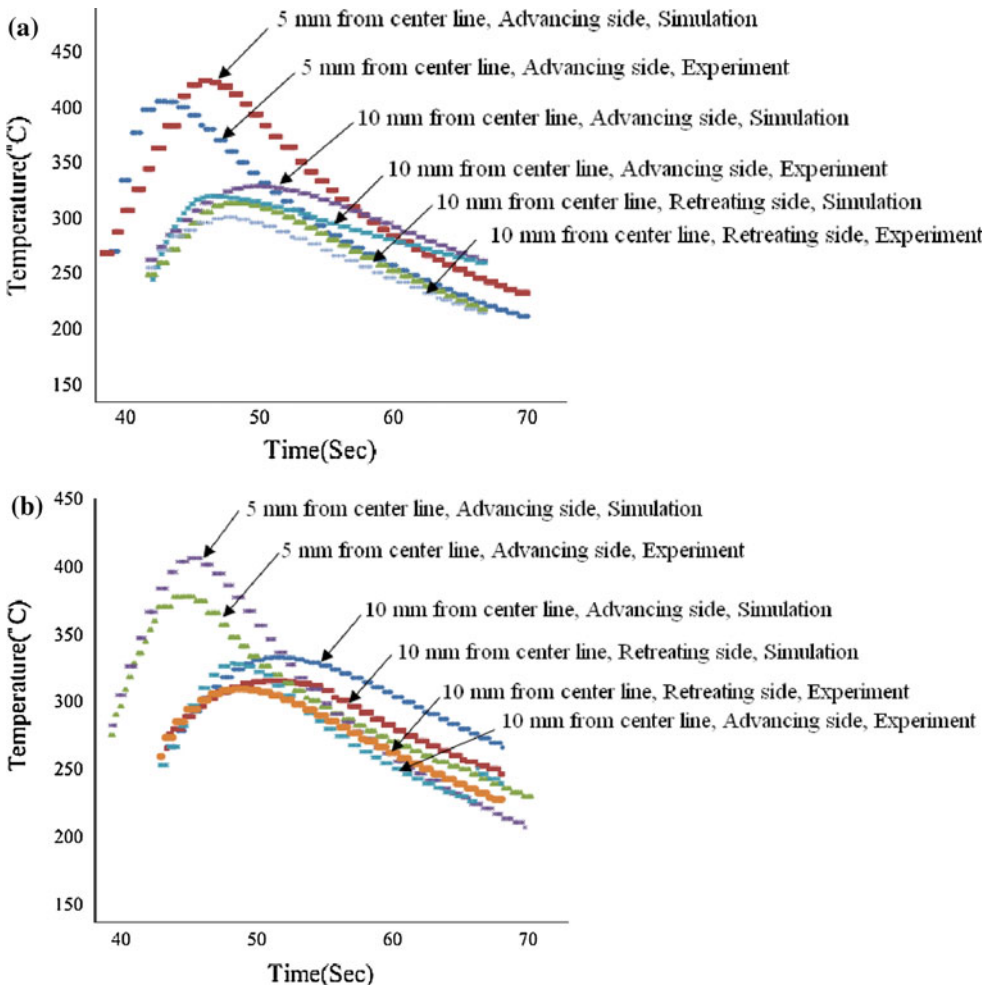

Fig. 6 Comparison between the experimental and the predicted thermal cycles in the various points; **a** sample B, **b** sample J

micro-hardness of the weld zone was measured on a cross-section perpendicular to the welding direction at 2 mm from the bottom side using 100 gf load for 15 s. To determine the transversal and longitudinal strengths of the welded samples, tensile tests in the above directions were also conducted using an INSTRON machine and drawing speed of 1 mm/min while the tensile tests were prepared according to ASTM E8M. In this way, it is possible to determine changes in mechanical properties of the welded alloys after welding operation.

Results and discussion

It is noteworthy that experiments were performed with rotational speed in the range of 600–1200 rpm and welding speed 10–15 cm/min but the experiments with two rotational speed 840 and 900 rpm in combination with welding speed 10 and 15 cm/min were found to be satisfactory. Examination of weld joints listed in Table 3 showed that tunnel-type defects exist within the welded samples E to H and M to T. Where in low tool rotational speed, i.e.,

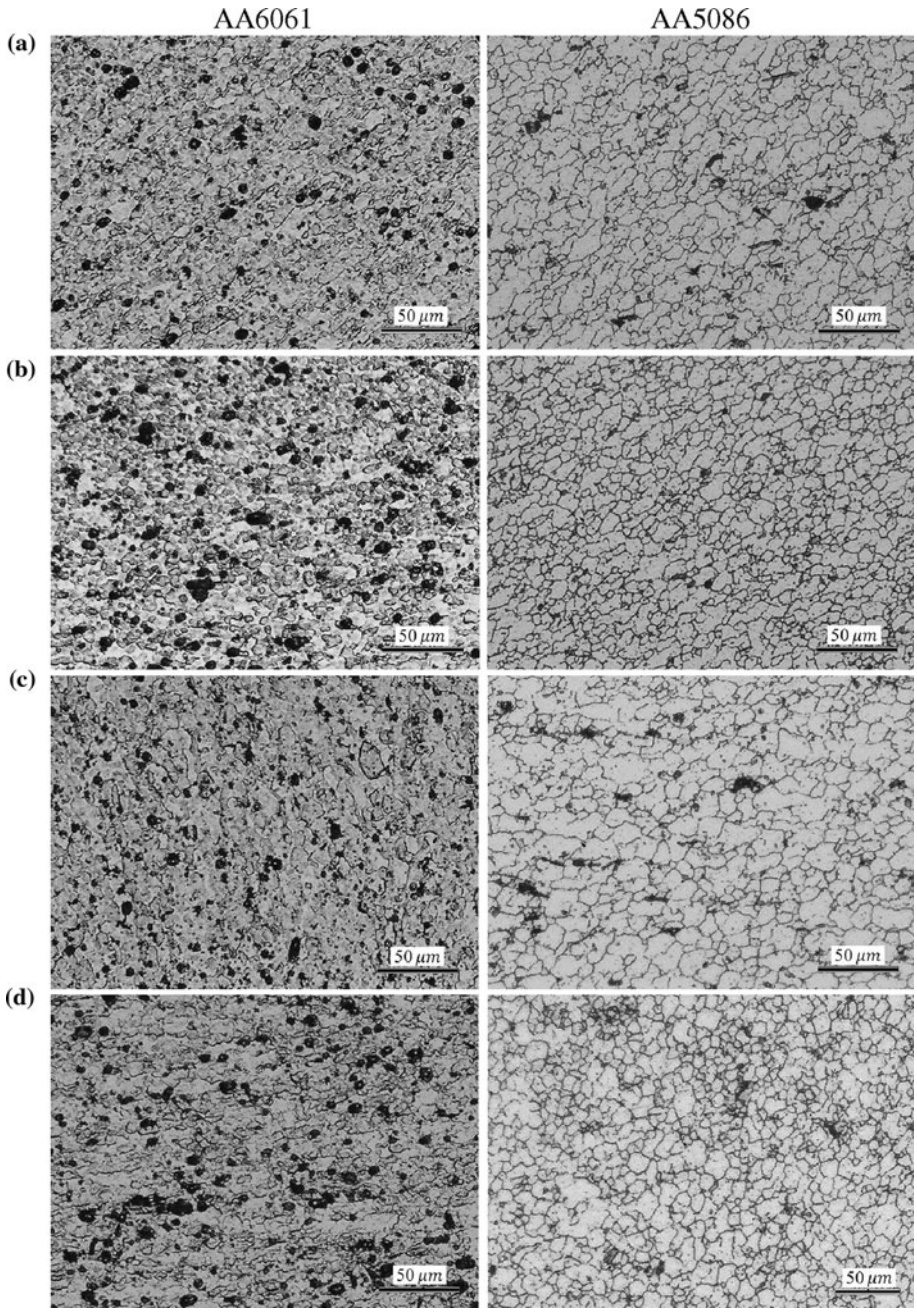

Fig. 7 Microstructures of the weld nugget under different welding conditions; **a** sample A, **b** sample B, **c** sample I, **d** sample J

samples Q to T in Table 3, insufficient material transportation as well as low heat generation by plastic deformation and friction at tool/work-piece interface may be responsible for producing defects. On the other hand, in high tool rotational speed, i.e., samples E to H and M to P in Table 3, high amount of heat input and the resulting turbulence in stir zone may be result in defects in the stirred zone. Therefore, because of defect existence in these samples, the above experiments were excluded and the results and the modeling of the other samples were only considered and discussed.

Figure 3 shows the top surface temperature fields after 15 s for the samples D and L. It can be seen that temperature gradients increases in front of the tool comparing to the wake of the weld, however, the larger thermal diffusivity of AA6061 results in higher amount of heat input flows within the AA6061 side. Even for the condition that AA5086 locates in the advancing side, although maximum temperature is observed close to the weld center line in the AA5086 side, however, a larger region is affected in the AA6061 side because of higher thermal diffusivity of AA6061 as shown in Fig. 3b. Figure 4 shows the temperature fields of samples A, B, I, and J in the cross-section transverse to the joint-line close to the tool/matrix interface after 15 s. It is observed that for all sample, the maximum temperature under tool/work-piece interface is higher in the advancing side compared to that in the retreating side. The higher plastic strain and heat of deformation leads to higher temperature in the advancing side close to the weld center line. Figure 5 shows recorded thermal cycles in the various points of samples C, D, K, and L at the depth of 2.5 mm. As it is expected the peak temperatures are higher at locations close to the weld line and it decreases toward the heat affected zone. Figure 6 compares the predicted and the measured temperature cycles. It is seen that there is a reasonable agreement between the two sets of results. It should be noted that the average difference between the numerical and the experimental maximum temperatures is

Table 4 Grain size of stirred zone and mechanical properties of FS-welded samples from tensile tests

Transversal direction		Stirred zone		Stirred zone grain size(μm)		
Yield stress (MPa)	Tensile strength (MPa)	Yield stress (MPa)	Tensile strength (MPa)	AA6061 side	AA5086 side	
114	223	131	236	7.4	10.1	Sample A
115	220	145	231	4.2	5.0	Sample B
107	231	124	248	12.2	13.4	Sample C
113	225	136	241	5.9	6.8	Sample D
116	218	130	233	10.3	12.5	Sample I
118	222	144	228	5.3	6.4	Sample J
104	228	122	236	12.8	14.5	Sample K
114	221	133	238	6.3	9.2	Sample L

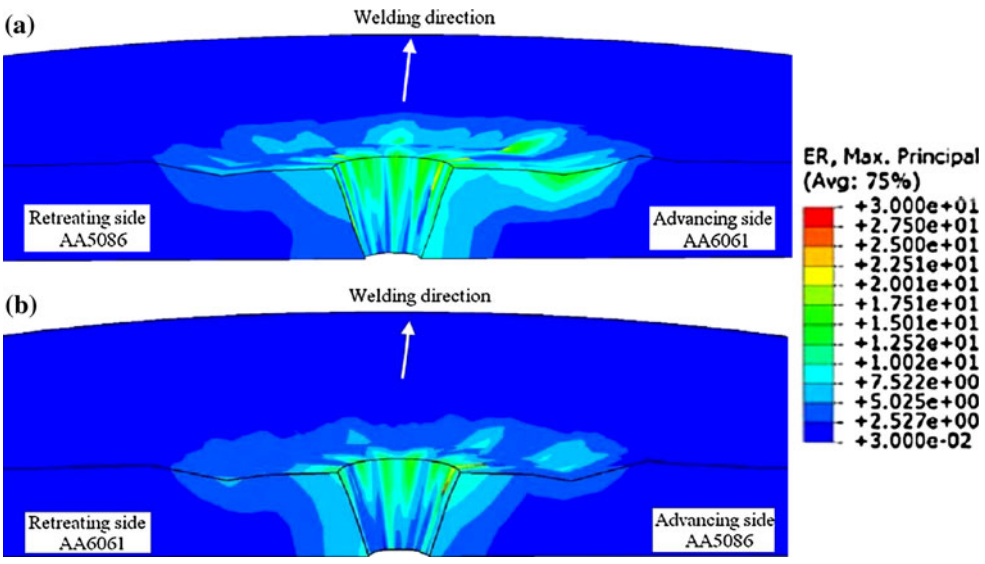

Fig. 8 Predicted strain rate distribution for; **a** sample A, **b** sample I

about 25 °C. The difference between these results may be due to the material parameters used in the numerical simulation, error in the experimental measurement of temperature, and ignoring the effect of material mixture in the weld nugget.

Both experimental and predicted peak temperatures are higher on the advancing side comparing to that in the retreating side, as shown in Fig. 6 demonstrating asymmetry distribution of temperature. It is worth mentioning that the average difference between the maximum temperatures in the advancing and the retreating sides is measured about 26.5 °C and the highest peak temperature occurs when AA6061 locates in the advancing side. Also, it is found that the longitudinal speed has a less significant effect on the peak temperature than rotational speed for the welding conditions employed in this work. For example, according to Figs. 5 and 6, it can be concluded that in constant rotational speed of 900 rpm, e.g., samples C and D, when welding speed increases from 10 to 15 cm/min the peak temperature decreases from 467 to 453 °C in the other hand, in constant welding speed of 15 cm/min, e.g., samples B and D, when rotational speed decreases from 900 to 840 rpm the peak temperature decreases consequently from 453 to 404 °C.

The microstructures of weld nugget under different working conditions are shown in Fig. 7. Microstructures of stirred zone consist of fine equiaxed grains in all samples and finer grains are produced in AA6061 comparing to AA5086 as shown in Fig. 7 and Table 4. It can be seen that the at lower longitudinal speed, e.g., 10 cm/min, larger grains form in the weld nugget both in AA5086 and AA6061 that it may be due to higher heat input produced at lower linear speeds leading to coarser recrystallized structures [22]. Figure 8 shows the predicted distribution of maximum principle strain rate for samples "A" and "I". The predictions show that the region affected by higher deformation rate is larger when AA6061 locates in the advancing side as displayed in this Fig. 8a. This may be attributed to the lower flow stress of AA6061 at high temperatures leading to material flows more readily. Additionally, it can be concluded the strain rate is distributed more uniformly if AA5086 locates in the advancing side which it means material mixing can be performed more efficiently under these circumstances.

Figure 9 shows that the mixing of material in stirred zone. It is seen that more efficient mixing is made when AA5086 is in the advancing side. It may be attributed to higher flow stress of AA5086 than AA6061 at all strain rates and temperatures in the range of 300–450 °C [19]. While AA5086 is in the retreating side, its flow behavior is affected by the low temperatures while if AA5086 is placed in the advancing side metal flow occurs more readily due to higher temperatures in this region. It should be noted that the similar results have been reported in other works [11, 23]. It is interesting to note that with increasing rotational speed of tool and decreasing traveling speed in the range considered in this work, mixing of materials increases regarding experimental observation of weld cross-section profiles shown in Fig. 9.

Figure 10 displays the hardness profile across the joints measured at 2 mm from the root face where AA5086-O and AA6061-T6 base metals show Vickers hardness of about 62 and 101, respectively. In the AA6061 side an abrupt decrease in hardness can be observed which may be attributed to the imposed thermal cycles as well as severe hot deformation. These lead to elimination of the precipitation hardening effect in the alloy owing to partial and/or complete dissolution of the hardening particles as shown in Fig. 11. For example, micro-hardness of sample "K" decreases from 97 to 65 in the TMAZ. However, near the weld center line, the hardness values increase again. In this region the microstructure of the weld is characterized by fine and equiaxed grains as shown in Fig. 9 and as a result,

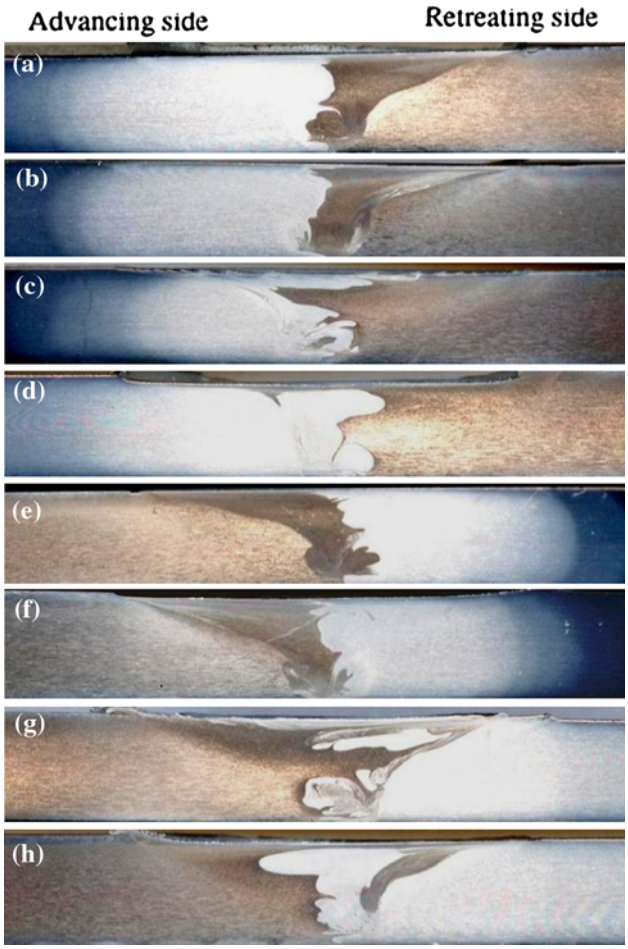

Fig. 9 Macrostructure of welded samples; **a** sample A, **b** sample B, **c** sample C, **d** sample D, **e** sample I, **f** sample J, **g** sample K, **h** sample L

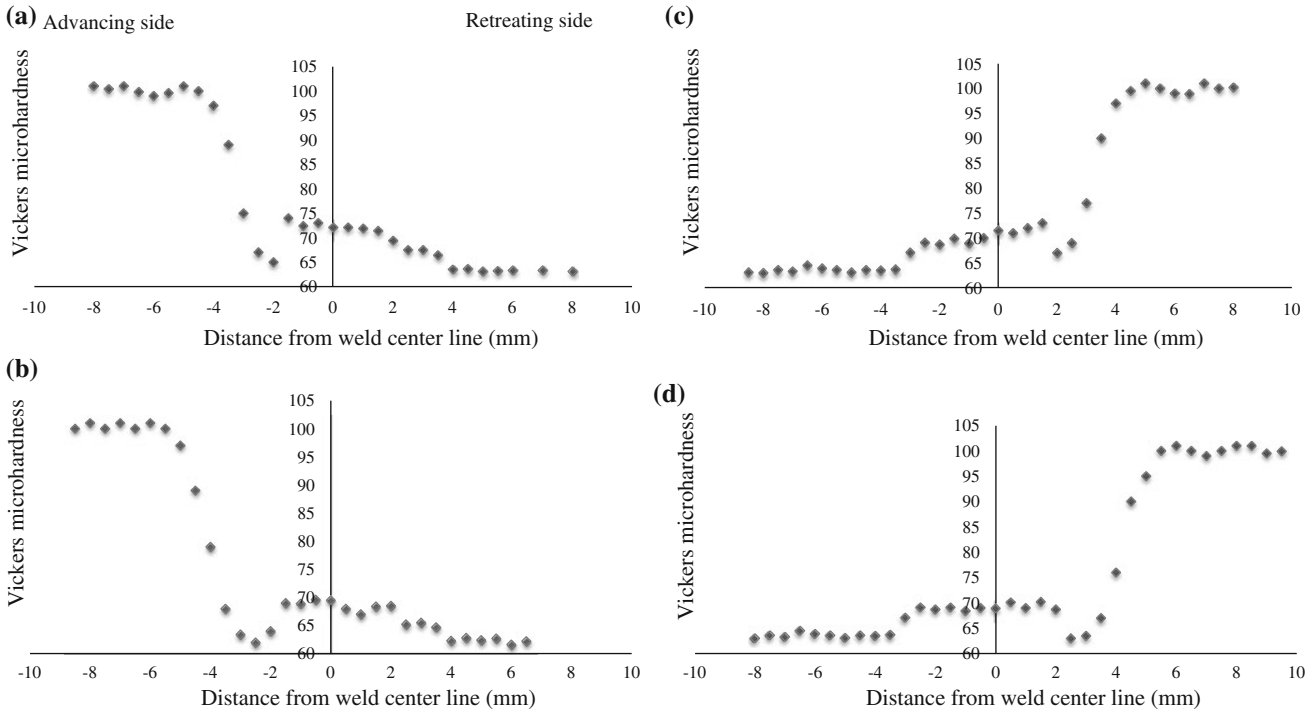

Fig. 10 Micro-hardness profile produced after FSW in; **a** sample B, **b** sample C, **c** sample J, **d** sample K

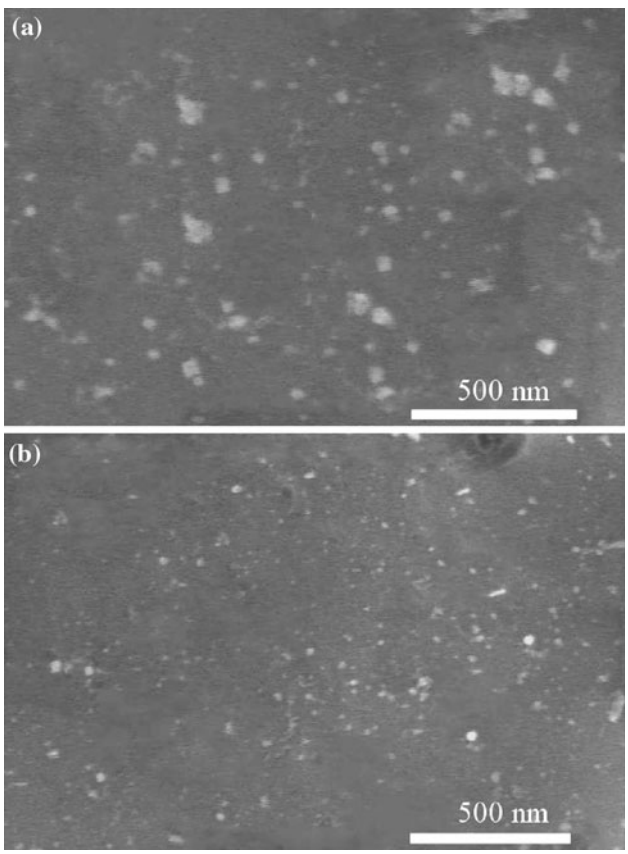

Fig. 11 SEM micrographs for the retreating side of sample L; **a** TMAZ, **b** stirred zone

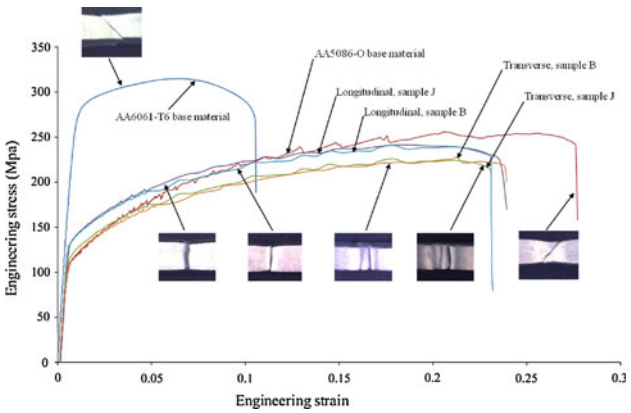

Fig. 12 Stress–strain behavior of transverse and longitudinal tensile specimen for samples B and J

Table 5 Mechanical properties of base material achieved from tensile tests

Yield stress (MPa)	Tensile strength (MPa)	
112	253	AA5086-O base material
278	315	AA6061-T6 base material

it increases the yield stress as well as the hardness. In all samples Vickers hardness in the weld nugget of AA6061 side is higher than AA5086 side, For example micro-hardness of sample "K" at AA6061 side and AA5086 side of weld nugget are about 71 and 69, respectively. It is may

be due to existence of the hardening precipitates as well as finer grain size of AA6061.

The results of the tensile tests for all samples are shown in Tables 4 and 5. The longitudinal samples extracted from the stirred zone show higher yield stress than that of the AA5086-O conditions. After yielding, the hardening behavior of the stirred zone becomes very similar to that of the softer AA5086-O base material as displayed in Fig. 12. The transverse and longitudinal tensile samples of stirred zone show almost the same ductility but the yield strength in longitudinal samples is higher. Note that in transverse samples fracture occurs in TMAZ of AA6061-T6 side where the sudden changing in hardness is observed.

Conclusions

Thermo-mechanical responses in dissimilar friction stir welding of AA5086/AA6061 have been analyzed using a thermo-mechanical model. In addition, utilizing the results of the model as well as the data achieved from the experimental testing, the microstructure, and mechanical behavior of dissimilar friction stir welded samples have been evaluated. The results can be summarized as follows:

1. In the all welded samples, the microstructure of weld nugget in AA6061 side shows finer grain size comparing to AA5086 side.
2. The temperature field in dissimilar FSW of AA5086/AA6061 is distributed asymmetrically producing larger thermally affected region in the AA6061 side.
3. The hardness variation across the dissimilar weld varies in a complex manner. In the AA5086 side, because of recrystallization and generation of fine grains in weld nugget the micro-hardness is higher than base metal but in the AA6061 side, because of dissolution of the hardening phases in the TMAZ softening has been observed. Although, in the weld nugget due to generation fine grain structure as well as greater volume fraction of hardening precipitates, softening is less than in TMAZ.
4. As the tool rotational speed increases and traveling speed decreases the mixing of material is made more efficiently.
5. In dissimilar FSW of AA5086-O/AA6061-T6 the mechanical properties of welded samples are more similar to AA5086-O base material and in conditions that AA5086 located in advancing side better mixing of material in stirred zone and higher yield strength were observed.

References

1. Thomas WM, Nicholas ED, Needham JC, Murch MG, Templesmith P, Dawes CJ (1991) Friction stir welding. International Patent Application No. PCT/GB92102203 and Great Britain Patent Application No. 9125978.8
2. Nicholas ED, Thomas WM (1998) Int J Mater Prod Technol 13:45
3. Woo W, Choo H, Withers PJ, Feng Z (2009) J Mater Sci 44:6302. doi:10.1007/s10853-009-3868-y
4. Safarkhanian MA, Goodarzi M, Boutorabi SMA (2009) J Mater Sci 44:5452. doi:10.1007/s10853-009-3735-x
5. Zhou L, Liu HJ, Liu QW (2010) J Mater Sci 45:39. doi:10.1007/s10853-009-3881-1
6. Venkateswaran P, Zhi-Hui Xu, Xiaodong Li, Reynolds AP (2009) J Mater Sci 44:4140. doi:10.1007/s10853-009-3607-4
7. Chen T (2009) J Mater Sci 44:2573. doi:10.1007/s10853-009-3336-8
8. Leal RM, Leitpo C, Loureiro A, Rodrigues DM, Vilaça P (2008) Mater Sci Eng A 498(1–2):384
9. Lee CY, Lee WB, Kim JW, Choi DH, Yeon YM, Jung SB (2008) J Mater Sci 43:3296. doi:10.1007/s10853-008-2525-1
10. Shigematsu I, Kown YJ, Suzuki K, Imai T, Saito N (2003) J Mater Sci Lett 22:353
11. Larsson H, Karlsson L, Stoltz S, Bergqvist E-L (2000) Joining of dissimilar al-alloys by friction stir welding, second international conference on friction stir welding. Gothenburg, Sweden, 26–28 June
12. Peel MJ, Steuwer A, Withers PJ, Dlckerson T, Shi Q, Sherclif H (2006) Metall Mater Trans A 37:2183
13. Peel MJ, Steuwer A, Withers PJ (2006) Metall Mater Trans A 37:2195
14. Steuwer A, Peel MJ, Withers PJ (2006) Mater Sci Eng A 441:187
15. Hibbit D, Karlsson B, Sorenson P (2004) Abaqus/Explicit user's manual, version 6.5. Abaqus Inc, Pawtucket, RI, USA
16. Belytschko T, Liu WK, Moran B (2000) Nonlinear finite element methods for continua and structures. Wiley, Chichester, England
17. Stasa FL (1985) Applied finite element method, chapters 10. CBS Publishing Ltd, Japan
18. Schmidt H, Hattel J (2005) Model Simul Mater Sci Eng 77–93
19. Prasad YVRK, Sasidhara S (1997) Hot working guide: a compendium of processing maps. ASM International, Materials Park, OH, USA, p 101
20. Chao Y, Qi X (1998) J Mater Proc Manuf Sci 7:215
21. Kim D, Badarinarayan H, Kim JH, Kim C, Okamoto K, Wagoner RH, Chung K (2010) Eur J Mech A 29:204
22. Humphreys FJ, Hatherly M (2004) Recrystallization and related annealing phenomena, 2nd edn. Elsevier, Oxford
23. Kumagai M (2001) Joining dissimilar alloys between AA5083 and A6NO1 by friction stir welding. 3rd international symposium on FSW, Kobe, Japan